Revision 4

Evaluation of residual pressure in an inclusion–host system using negative frequency shift of quartz Raman spectra

Yui Kouketsu,[1,*] Tadao Nishiyama,[2] Takeshi Ikeda,[3] and Masaki Enami[4]

[1]Department of Earth and Planetary Sciences, Nagoya University, Nagoya 464-8601, Japan

[2]Department of Earth and Environment, School of Science, Graduate School of Science and Technology, Kumamoto University, 2-39-1 Kurokami, Kumamoto 860-8555, Japan

[3]Department of Earth and Planetary Sciences, Graduate School of Science, Kyushu University, 33 Hakozaki, Fukuoka 812-8581, Japan

[4]Center for Chronological Research, Nagoya University, Nagoya 464-8602, Japan

*Corresponding author:

Email address: kouketsu.yui@nagoya-u.jp

Present address: Geochemical Research Center, Graduate School of Science, The University of Tokyo, Tokyo 113-0033, Japan

Running title: Evaluation of negative residual pressure of quartz in garnet

ABSTRACT

Raman spectra of quartz inclusions in garnet hosts of low-pressure/temperature metamorphic rocks from the Yanai district in the Ryoke belt (around 0.1–0.3 GPa/500–600 °C), Southwest Japan, exhibit frequency (peak position) shifts towards lower wavenumbers as compared to those of a quartz standard measured at ambient conditions. The observed negative frequency shifts indicate that tensile normal stress is exerted on the quartz–garnet boundary and therefore, quartz inclusions are subjected to negative residual pressure. Elastic modeling that assumed the constant elastic properties of minerals cannot explain this negative residual pressure. This study estimated the residual pressure based on a new scheme of elastic modeling with equation of state (EOS) of quartz and garnet, which takes into account the pressure- and temperature-dependency of compressibility and expansivity. The calculated residual pressure was converted into frequency shifts of quartz Raman spectrum based on the

experimentally determined relation. The results showed that the quartz inclusions in garnets retain residual pressure of about -0.3 GPa, and logically reproduced the observed frequency shifts in the direction of lower wavenumbers. The new elastic modeling also simulates positive frequency shifts retained by quartz inclusions in garnets of high-pressure metamorphic rocks from the Sambagawa metamorphic belt in Southwest Japan, and from the Motagua fault zone in Guatemala. The degree and direction of Raman frequency shifts of quartz inclusion in garnet depend on metamorphic conditions when the quartz was included in the host garnet. Conversely, the metamorphic conditions prevailing when a set of a quartz inclusion and garnet host was recrystallized can be inferred from Raman frequency shifts of quartz inclusion in garnet. The proposed Raman spectroscopic analysis should be a powerful and useful tool to decipher information at earlier stage of garnet growth even in samples of highly recrystallized matrix phases during exhumation and retrograde stages.

Keywords: Raman spectroscopy; negative residual pressure; Ryoke metamorphic rocks; quartz; garnet; equation of state

INTRODUCTION

Mineral or fluid inclusions within host minerals preserve information related to the metamorphic history during the growth of the host mineral. In general, these metamorphic conditions are constrained using mineral reactions or thermodynamic calculations based on the analysis of the chemical compositions of the host and inclusion (e.g., Whitney et al. 1995; Katayama et al. 2000; Tsunogae and Santosh 2006). On the other hand, the physical properties of the host and inclusion can also be used to estimate the metamorphic conditions. One of those techniques involves the analysis of residual pressure. Each mineral has distinct compressibility and expansivity characteristics. Consequently, after inclusion is incorporated to the host mineral, both phases will follow different volume change paths according to change in surrounding pressure (P)–temperature (T) conditions. This volume difference in the inclusion–host system, designated as residual pressure (or internal stress), can be detected as a change in the Raman frequencies (i.e. peak positions) and/or widths (e.g., Hemley 1987; Parkinson and Katayama 1999; Nasdala et al. 2005; Kagi et al. 2009). Raman spectroscopy can analyze confined materials without sample destruction if the sample is transparent to visible light. Therefore, this technique is appropriate for detecting the residual pressure preserved in the inclusion within the host mineral. Izraeli et al. (1999) detected the residual pressure by measuring the Raman frequency shifts of olivine

72 inclusions in diamond from the Udachnaya mine in Siberia, and estimated the
73 metamorphic pressure using bulk modulus, shear modulus, and thermal expansion
74 parameters of inclusion and host minerals. Sobolev et al. (2000) also detected the
75 residual pressure by measuring the Raman frequency shifts of small coesite inclusions
76 in diamond from Venezuela, and estimated the initial pressure of the diamond formation.
77 The results of these two studies are consistent with the diamond stability field.
78 Enami et al. (2007) detected the residual pressure by measuring the Raman
79 frequency shifts of quartz inclusions in garnets metamorphosed at three different
80 metamorphic facies: amphibolite, epidote-amphibolite, and quartz-eclogite. They
81 confirmed that the Raman peaks of quartz inclusions shift to higher wavenumber side
82 with increasing the metamorphic pressure, which implies that the values of residual
83 pressures of quartz inclusions increase with increasing the metamorphic pressure. This
84 approach is very convenient because the combination of garnet and quartz is common in
85 metasedimentary rocks. However, several problems are inherent in the study reported by
86 Enami et al. (2007): (1) the degree of Raman frequency shifts of quartz inclusions in
87 garnets was compared only among three different metamorphic facies conditions,
88 whereas those of the other metamorphic conditions are unclear; and (2) the elastic
89 modeling applied to estimate the metamorphic pressure from the residual pressure was

too simplified and the accuracy for quantitative estimation of the metamorphic condition has not been sufficiently verified yet.

Recently, some studies have examined the residual pressure of quartz inclusions in garnets from high- to ultra-high temperature metamorphic rocks. Sato et al. (2009) reported the Raman spectrum of a quartz inclusion in garnet from ultra-high temperature metamorphic rock in Kumiloothu, southern India. The Raman peaks of this quartz inclusion show lower wavenumbers than those of quartz at ambient conditions, which implies that the interface between the quartz inclusion and garnet host is subjected to a tensile normal stress, and that the quartz inclusion in garnet of ultra-high temperature metamorphic rock preserves negative residual pressure. Nishiyama and Aikawa (2011) also reported the negative frequency shifts of Raman spectra, i.e. negative residual pressures, of quartz inclusions in garnets from high-*T* Higo metamorphic rocks, Southwest Japan. In a study by Enami et al. (2007), the residual pressure of quartz in garnet was numerically modeled with respect to the metamorphic *P*–*T* conditions, based on a "spherical inclusion model" (Van der Molen 1981), in which the elastic properties of minerals were treated as independent of pressure and temperature. By applying this model to a quartz inclusion–garnet host system, the residual pressure becomes negative only under conditions of extremely low-*P*/*T*. The estimated metamorphic condition of

the Higo terrane was not within this calculated negative range. Therefore, Nishiyama and Aikawa (2011) attributed the negative frequency shifts of quartz Raman spectra of their samples to drastic volume reduction of quartz in the transition from β to α phases during the retrograde stage.

In this study, we discovered quartz inclusions showing negative Raman frequency shifts in garnets from high-*T* and low-*P* metamorphic rocks in the Ryoke belt, Southwest Japan, which never reached the β-quartz stability field. This feature can be explained neither by phase transition nor by the spherical inclusion model with constant elastic properties. Therefore, we recalculated the residual pressure of quartz in garnet, considering the *P*–*T* dependency on compressibility and expansivity, by employing the equation of state (EOS) of quartz and garnet (Holland and Powell 1998; Plymate and Stout 1989). Subsequently, we converted the calculated residual pressure into Raman frequency shifts based on the experimental dataset of Schmidt and Ziemann (2000) and constructed the relationship diagram of pressure-temperature-Raman frequency shifts of quartz inclusion in garnet. The accuracies of calculated residual pressure and Raman frequency shifts were verified by comparing the measured Raman frequency shifts of quartz inclusions reported here and in previous studies (Kouketsu et al., 2010; Endo et

al., 2012). Based on these discussions, we examined the quantitative constraint of metamorphic conditions from the Raman frequency shifts of quartz inclusion in garnet.

SAMPLE DESCRIPTION

The Ryoke belt in Southwest Japan, which mainly comprises Cretaceous Ryoke granitoids and associated metamorphic rocks of low-*P* facies series, has been regarded as a typical example of a low-*P* and high-*T* metamorphic belt (Miyashiro 1961), where andalusite and sillimanite occur in medium- and high-grade areas, respectively.

In the Yanai district, the Ryoke metamorphic rocks are derived mainly from pelites, psammites, and cherts, with subordinate amounts of calcareous and basic rocks, which are regarded as belonging to the Jurassic accretionary complex (Higashimoto et al. 1983). Cretaceous granitic rocks, which intruded extensively into these protoliths, are divided into three suites: the Older Ryoke, the Younger Ryoke, and the San-yo granitic rocks, in order of intrusion (Fig. 1). The first suite is syn-metamorphic whereas the latter two suites are post-metamorphic (e.g., Suzuki and Adachi 1998). The dominant pelitic rocks display metamorphic zonation on a regional scale. Ikeda (1998) defined the following metamorphic zones in ascending metamorphic grade: chlorite (Chl), chlorite-biotite (Chl-Bt), biotite (Bt), muscovite-cordierite (Ms-Crd),

143 K-feldspar-cordierite (Kfs-Crd), sillimanite-K-feldspar (Sil-Kfs), and garnet-cordierite
144 (Grt-Crd) zones (Fig. 1).

145 Ikeda (2004) determined *P–T* conditions of these zones using thermodynamic
146 methods of garnet–biotite geothermometers and garnet–Al-silicate–plagioclase (GASP)
147 geobarometers with the thermodynamic dataset of Holland and Powell (1998). In this
148 study, six garnet-bearing samples were studied: YEB5 from Chl-Bt zone; YBB7, YMA5,
149 YAM10 from Ms-Crd zone; and YAF16, YAF19 from Kfs-Crd zone (Fig. 1; Table 1).
150 The *P–T* condition of the sample YEB5 from Chl-Bt zone was estimated at 0.08
151 GPa/492 °C. The localities of the three samples from Ms-Crd zone (YBB7, YMA5,
152 YMA10) were within 200m from that of YBB6, for which 0.19 GPa/551 °C were
153 estimated. The *P–T* conditions of the samples YAF16 and YAF19 from Kfs-Crd zone
154 were estimated at 0.26 GPa/594 °C and 0.27 GPa/590 °C, respectively. The
155 metamorphic conditions of these samples are in the α-quartz stability field. The
156 uncertainties in these conditions are derived mainly from analytical errors in the
157 analyses of the mineral composition, and are 0.1 GPa and 35 °C (Ikeda 2004). All
158 samples are pelitic rocks except YAF16, which is siliceous.

159

160 **EXPERIMENTAL PROCEDURES AND QUARTZ RAMAN SPECTRA**

Measurements were performed using a Thermo Scientific Nicolet Almega XR Raman spectrometer available at the Petrology Laboratory of Nagoya University. The Raman spectra were collected with an Olympus BX51 automated confocal microscope, using an Olympus Mplan-BD 100X (NA=0.9) objective. The Raman scattering was excited with an Nd:YAG laser emitting at 532 nm. The output laser power was 25 mW, while the irradiation power on the sample surface of approximately 10mW. The suppression of the Rayleigh scattering was achieved with a notch filter. The scattered light was analyzed with a grating of 2400 lines/mm and it was detected with a Peltier-cooled CCD camera (256×1024 pixels; Andor Technology). The room temperature was kept at 22 ± 1 °C. The lateral spatial resolution was about 1 μm. The spectral resolution was about 1 cm^{-1}. The spectrograph was calibrated using the plasma lines of a neon lamp.

As can be seen in Fig. 2, intense peaks in the Raman spectrum of α-quartz are near 464, 205, and 128 cm^{-1} at ambient condition (e.g., Dean et al. 1982; Schmidt and Ziemann, 2000; Enami et al. 2007). The peaks near 464 and 205 cm^{-1} originate from A_1 modes, whereas the peak near 128 cm^{-1} arises from an E mode in α-quartz (Etchepare et al. 1974). We refer to the peaks near 464, 205, and 128 cm^{-1} at ambient conditions as $A_{1(464)}$, $A_{1(205)}$, and $E_{(128)}$, respectively (Fig. 2). The positions of these peaks shift to

179 higher wavenumbers when quartz is subjected to compressive stress, and shift to lower
180 wavenumbers when quartz is subjected to tensile stress (Gallivan and Gupta 1995).
181 Enami et al. (2007) evaluated the extent of frequency shifts of quartz Raman spectrum
182 using the difference of wavenumbers between α-quartz standard and sample to avoid
183 systematic errors: $\Delta\omega_1 = \omega_1^{\text{standard}} - \omega_1^{\text{sample}}$ and $\Delta\omega_2 = \omega_2^{\text{sample}} - \omega_2^{\text{standard}}$, where ω_1 and ω_2
184 denote the difference of wavenumbers between $A_{1(464)}$ and $A_{1(205)}$, and $A_{1(205)}$ and $E_{(128)}$,
185 respectively. In this study, the Raman spectrum of euhedral pegmatitic α-quartz reported
186 in Enami et al. (2007) was used as a standard. The values of $\Delta\omega_1$ and $\Delta\omega_2$ are positive
187 when quartz is subjected to compressive stress, and negative when quartz is subjected to
188 tensile stress. The standard deviations of $\omega_1^{\text{standard}}$ and $\omega_2^{\text{standard}}$ in α -quartz standard
189 are ±0.3 cm^{-1} (Enami et al. 2007).
190

191 **SAMPLE MEASUREMENT**

192 Raman spectra were measured from a petrographic thick section (about 100 μm
193 thick). Quartz inclusions that were exposed neither on the side of the polished surface
194 nor on the glass slide were selected. We also avoided quartz in the fractured host
195 because the frequency shift of such a sample becomes smaller than that of quartz
196 completely surrounded by unfractured host (Fig. 3; Enami et al. 2007).

Negative frequency shifts of quartz Raman spectra were obtained from all studied samples (Fig. 4; Table. 1). The quartz inclusions of the sample YEB5 (Chl-Bt zone) showed frequency shifts of $\Delta\omega_1$ = -1.5 to -4.5 cm^{-1} and $\Delta\omega_2$ = -1.3 to -4.2 cm^{-1} (Fig. 4a). The quartz inclusions of Ms-Crd zone showed $\Delta\omega_1$ = -0.1 to -4.0 cm^{-1} and $\Delta\omega_2$ = 0.5 to -3.1 cm^{-1} in YBB7; $\Delta\omega_1$ = -0.2 to -3.2 cm^{-1} and $\Delta\omega_2$ = 0.4 to -2.8 cm^{-1} in YMA5; and $\Delta\omega_1$ = -0.4 to -2.9 cm^{-1} and $\Delta\omega_2$ = -0.2 to -1.7 cm^{-1} in YMA10 (Fig. 4b). The quartz inclusions of Kfs-Crd zone showed $\Delta\omega_1$ = 0.2 to -3.9 cm^{-1} and $\Delta\omega_2$ = 0.8 to -3.0 cm^{-1} in YAF16; and $\Delta\omega_1$ = -0.3 to -4.4 cm^{-1} and $\Delta\omega_2$ = 1.0 to -4.1 cm^{-1} in YAF19 (Fig. 4c).

ELASTIC MODELING OF RESIDUAL PRESSURE

Fundamental equation

To examine the generation mechanism of negative residual pressure, numerical calculations based on elastic modeling were conducted. We evaluated the normal stress (radial stress) component at the inclusion–host boundary as residual pressure. The residual pressure in the inclusion–host system has been determined by numerical simulation based on theory of linear elasticity in several studies using the relative volume changes of inclusion and host minerals (e.g., Gillet et al. 1984; Van der Molen and Van Roermund 1986; Zhang 1998; Guiraud and Powell 2006). We assumed that (1)

the inclusion and host are concentric spheres, (2) the inclusion and host are elastically isotropic, (3) the size of inclusion is much smaller than that of the host mineral, and (4) the inclusion is sufficiently distant from other inclusions and from the edge of the host. Following the previous study of Guiraud and Powell (2006), the volume ratio of the initial *P*–*T* condition (P_0, T_0) and arbitrary *P*–*T* condition (P, T) for the host mineral is given by the following relation:

$$\frac{V_h(P,T)}{V_h(P_0,T_0)} = \frac{V_i(P_i,T)}{V_i(P_0,T_0)} - \frac{3}{4\mu}(P_i - P) \qquad \text{(Equation 1)}$$

where V represents volume and μ is the shear modulus of the host mineral. The subscript "*h*" represents the host; "*i*" represents the inclusion; and "0" represents the conditions at which the inclusion has been incorporated into the host mineral. Because the inclusion and host minerals undergo different volume changes, the pressure on the inclusion (P_i) at the arbitrary *P*–*T* condition differs from the external pressure (P). The term P_i at standard condition corresponds to the residual pressure that we want to know. In this study, we use this fundamental equation to estimate the residual pressure at

atmospheric pressure and room temperature (P_i at P = 0.1 MPa and T = 25 °C) from the arbitrary metamorphic condition (P_0, T_0).

Derivation of residual pressure

In order to derive the residual pressure using Equation 1, the volumes of quartz and garnet crystals have to be evaluated. The equation of state (EOS) model employed by Holland and Powell (1998) was examined:

$$V(P,T) = V(0.1\text{MPa},298\text{K})\left[1 + a°(T-298) - 20a°(\sqrt{T} - \sqrt{298})\right] \times \left[1 - \frac{4P}{\kappa\left\{1 - 1.5\times10^{-4}(T-298)\right\} + 4P}\right]^{1/4} \quad \text{(Equation 2)}$$

where $a°$ is the thermal expansion parameter and κ is the bulk modulus at 298 K. The relation between the thermal expansion parameter $a°$ and thermal expansion coefficient α is expressed as $\alpha = a°(1 - 10/\sqrt{T})$. The datasets of the thermoelastic parameters in Holland and Powell (1998) are $a°$ = 0.65×10^{-5} K^{-1} and κ = 75.0 GPa for quartz; and $a°$ = 4.03×10^{-5} K^{-1} and κ = 169.0 GPa for almandine (Table 2). The thermoelastic parameters of almandine and the other garnet end-members in Holland and Powell (1998) are not so different from those reported in other studies (e.g., Fei 1995; Wang and Ji 2001), and

248 calculated volume change of garnet well matched the experimental data (e.g., Zhang et
249 al. 1999; Wang and Ji 2001; Pavese et al. 2001). Therefore, we adopted the volume
250 change of almandine using the EOS and thermoelastic parameters of Holland and
251 Powell (1998) for the derivation of residual pressure. On the other hand, the
252 thermoelastic parameters of quartz in Holland and Powell (1998) are extremely different
253 from the others (e.g., Fei 1995; Plymate and Stout 1989; Dorogokupets 1995), where
254 the thermal expansion parameter is one order of magnitude smaller and the bulk
255 modulus is twice as large as those of the others (Table 2), and calculated volume change
256 of quartz using the EOS model and thermoelastic parameters of Holland and Powell
257 (1998) did not match the experimental data (e.g., Ackermann and Sorrell 1974;
258 Jorgensen 1978; Ogata et al. 1987; Carpenter et al. 1998). Therefore, we recalculated
259 the volume change of quartz using the different thermoelastic parameters reported in
260 Plymate and Stout (1989; Fig. 5a) and in Dorogokupets (1995; Fig. 5b). For comparison,
261 we additionally calculated the volume change of quartz using the EOS model and
262 thermoelastic parameters reported in Plymate and Stout (1989; Fig. 5c), which derived
263 the EOS for solids using five parameters based on an exponential temperature correction
264 of the isothermal Murnaghan equation. The volume of α-quartz was calculated using the

following equation with the dataset of $\alpha = 3.13 \times 10^{-5}$ K^{-1}, $\alpha' = 6.97 \times 10^{-8}$ K^{-2}, $\kappa = 37.31$ GPa, $\kappa' = 6.37$, and $\partial\kappa/\partial T = -0.98 \times 10^{-2}$ GPa/K.

$$V(P,T) = V(0.1\,\mathrm{MPa},298\mathrm{K})\left[1+\frac{\left\{\kappa'(P-0.1\mathrm{MPa})+\left(\frac{\partial\kappa}{\partial T}\right)(T-298)\right\}}{\kappa}\right]^{-1/\kappa'} \times \exp\left[\left\{\alpha+\frac{\left(\frac{\partial\kappa}{\partial T}\right)}{\kappa\kappa'}\right\}(T-298)+\left\{\alpha'-\frac{\left(\frac{\partial\kappa}{\partial T}\right)^2}{\kappa^2\kappa'}\right\}\frac{(T-298)^2}{2}\right] \quad \text{(Equation 3)}$$

Results obtained using these three calculations (Figs. 5a–5c) matched the experimental data. Then we derived the residual pressure based on the calculated volumes of quartz in these three cases. Although quartz transforms from α- to β-phase at 574 °C at 0.1 MPa (e.g., Shen et al. 1993), we did not consider the phase transition of quartz because the *P*–*T* range considered in this study (0.1 MPa–2.6 GPa/25–600 °C) is mostly within the α-quartz stability field.

P_i can be derived by substituting Equation 2 or 3 into Equation 1 (Figs. 5d–5f). In those calculations, negative residual pressure appears at the low-*P*/*T* range. The estimated metamorphic conditions of the measured samples are within this range. These calculation results can explain the negative frequency shifts measured in Yanai Ryoke

metamorphic rocks. The calculation result of volume change of quartz using the EOS model and thermoelastic parameters reported by Plymate and Stout (1989; Fig. 5c) was most consistent with the experimental data (e.g., Ackermann and Sorrell 1974; Jorgensen 1978; Ogata et al. 1987; Carpenter et al. 1998). Therefore, the calculation result of residual pressure in Figure 5f will be used in the following discussion.

Conversion into $\Delta\omega_1$

The residual pressure P_i can be converted into $\Delta\omega_1$ and $\Delta\omega_2$. Schmidt and Ziemann (2000) investigated in-situ frequency shifts of quartz Raman spectra using a hydrothermal diamond-anvil cell. Following their experimental data, the relations between pressure (P; GPa) and frequency shifts ($\Delta\omega_1$ and $\Delta\omega_2$; cm^{-1}) are obtained:

$$\Delta\omega_1\ (cm^{-1}) = -3.47\ P^2 + 18.3\ P \text{ (correlation coefficient: } R^2 = 0.9995) \quad \text{(Equation 4)}$$

$$\Delta\omega_2\ (cm^{-1}) = -3.02\ P^2 + 20.5\ P\ (R^2 = 0.9997) \quad \text{(Equation 5)}$$

where 0.1 MPa < P < 2.1 GPa at 23 °C (Fig. 6). The above equations are based on the frequency shift at 0.1 MPa and 23 °C as standard and derived to pass through the origin. Although the experiment of Schmidt and Ziemann (2000) was conducted only under the

compressional condition, the tensile condition corresponding to negative residual pressure is also calculated by extrapolating the relation between pressure and the frequency shift in the lower compressional range. In a pressure range from 0.1 MPa to 0.45 GPa, the frequencies shift linearly with pressure (Fig. 6). They are expressed as shown below.

$$\Delta\omega_1\ (\mathrm{cm}^{-1}) = 17.1\ P \qquad \text{(Equation 6)}$$

$$\Delta\omega_2\ (\mathrm{cm}^{-1}) = 19.8\ P \qquad \text{(Equation 7)}$$

By extrapolating this equation to the negative range, the negative residual pressure will be evaluated.

FACTORS AFFECTING THE RESIDUAL PRESSURE

There are several factors that affect the value of residual pressure. We examined the effect of the following aspects on the residual pressure: (1) the grain size and shape of quartz inclusion, (2) the radius ratio between the inclusion and the host crystal, (3) the chemical composition of garnet host, and (4) the hydrolytic weakening. Based on these examinations, the variations of $\Delta\omega_1$ and $\Delta\omega_2$ values are considered.

316

317 **Grain size and shape of quartz inclusion**

318 Enami et al. (2007) reported a weak correlation between the frequency shifts and
319 grain size of quartz inclusions in garnets in the positive range. This result implies that
320 the negative frequency shifts of quartz inclusion are also affected by the grain size.
321 Therefore, we checked the relation between frequency shifts ($\Delta\omega_1$ and $\Delta\omega_2$) and mean
322 grain size ($\sqrt{ab}$), where *a* and *b* are longest and shortest lengths of quartz inclusions,
323 respectively (Figs. 7a and 7b). The mean grain size of measured quartz inclusions are
324 around 2–10 μm. No apparent correlation exists between the grain size and the values of
325 $\Delta\omega_1$ and $\Delta\omega_2$. In a study reported by Enami et al. (2007), the grain size of quartz
326 inclusions was 4–33 μm, which are larger than those in the present study. Therefore, the
327 effect of grain size might appear for quartz inclusions with mean grain size larger than
328 10 μm.

329 Burnley and Davis (2004) and Burnley and Schmidt (2006) reported that the volume
330 change of fluid inclusion that occurs with the pressure change is affected strongly by the
331 aspect ratio of the inclusion. Therefore, we also checked the relation between frequency
332 shifts and grain shape (aspect ratio; *b*/*a*) of quartz inclusions (Figs. 7c and 7d). The
333 shape of quartz inclusions varies, tending to show irregular shape in the lower-grade

zone, and tending towards spherical in the higher-grade zone (Figs. 3 and 7c,d). However, no apparent correlation was identified between grain shape and the values of $\Delta\omega_1$ and $\Delta\omega_2$. The effect of grain shape of solid inclusion might be much smaller than that of fluid inclusion in magnitude and also in the areal extent, and was not detected by the resolution of micro-Raman spectroscopy (Everall 2000a,b).

Radius ratio between the inclusion and host

Several studies have examined the effect of the radius of inclusion relative to the radius of the host mineral (Gillet et al. 1984; Van der Molen and Van Roermund 1986; Zhang 1998). Following the method of Zhang (1998), we recalculated the residual pressure using the equation considering the radius ratio between the inclusion and host:

$$\frac{V_h(P,T)}{V_h(P_0,T_0)} = \frac{V_i(P_i,T)}{V_i(P_0,T_0)} - \frac{(P_i - P)}{1-x}\left[\frac{x}{\kappa_h} + \frac{3}{4\mu}\right] \qquad \text{(Equation 8)}$$

where $x = R_i^3 / R_h^3$; R_i and R_h represent radii of the inclusion and host. When $x = 0$, Equation 8 becomes equal to Equation 1, meaning that the host radius is infinitely larger than that of the inclusion. When $x = 0.001$ and 0.01, the residual pressure is almost

identical as that in the case of $x = 0$ (Fig. 8). The residual pressure becomes slightly lower at positive, and higher at negative residual pressure region in the case of $x = 0.1$, in which the radius of the host garnet is approximately twice that of the quartz inclusion. The maximum differences in residual pressure in the cases of $x = 0$ and 0.1 were 0.05 GPa at 2.6 GPa/500 °C (Fig. 8a) and 0.04 GPa at 2.6 GPa/600 °C (Fig. 8b). In the measured samples, the radii of quartz inclusions are around 2–10 μm, whereas host garnet grains are around 50–300 μm. Therefore, the maximum value of x is close to 0.01, i.e., most of the quartz inclusions are sufficiently smaller than the host garnets. Although the actual measurement condition differs from the assumed ideal condition, in which the inclusion and host are concentric spheres and both phases are elastically isotropic, the effect of the radius ratio is regarded as slight.

Chemical composition of garnet host

The residual pressures estimated using the parameters of garnet end-members, almandine, pyrope, grossular, and spessartine, were compared. The datasets of thermal expansion parameters and bulk moduli of the garnet end-members were referred from Holland and Powell (1998), and shear moduli were from Wang and Ji (2001; Table 2). The residual pressure in the case of spessartine host was comparatively higher than

those of the other end-members (Fig. 9). The maximum difference was observed at 2.6 GPa/600 °C in the *P*–*T* range of 0.1 MPa–2.6 GPa/25–600 °C. The residual pressure at this condition was 1.10 GPa in the case of spessartine, whereas those of almandine, pyrope, and grossular were 1.01 GPa, 1.05 GPa, and 1.01 GPa, respectively.

Representative chemical compositions of garnets from the Yanai district are shown in Appendix Table 1. Since the content of spessartine component (X_{Sps}) in the garnets is relatively high; that is around 0.3 in Ms-Crd and Kfs-Crd zones and reaches 0.6 in Chl-Bt zone, the calculated residual pressure of quartz inclusion in garnet in the case of the almandine end-member host might be less than the residual pressure converted from the measured Raman frequency shifts of quartz inclusions from the Yanai district.

Hydrolytic weakening

The trace amount of water reduces the strength of silicates (e.g., Griggs 1967; Rossman 1990; Johnson 2006; Cao et al. 2011). The possibility exists that the residual pressure was released by hydrolytic weakening. However, Raman spectroscopy of the host garnets showed no OH-bond around 3600 cm^{-1}.

386 It appears that the grain size and shape (factor 1), inclusion-host radius ratio (factor
387 2), and hydrolytic weakening (factor 4) do not influence the residual pressure value. The
388 chemical composition of garnet host (factor 3) affects the difference of residual pressure
389 up to 0.1 GPa in the case of almandine and spessartine host, and this difference
390 corresponds to around 1 cm^{-1} for $\Delta\omega_1$ and $\Delta\omega_2$ values. However, the frequency shifts of
391 quartz inclusions range from around 0 to -4 cm^{-1} in all samples (Fig. 4). The four factors
392 described above seem not to be a major cause of this large variation from 0 to -4 cm^{-1}.
393 The other factor is that a quartz inclusion with a frequency shift close to zero might
394 release part or all the residual pressure through invisible cracking or dislocation. As
395 described above, the cause for dispersion of the measured frequency shift is unclear in
396 this study. However, we regard the quartz grain with the maximum frequency shift as
397 preserving valuable information related to the residual pressure reflecting the condition
398 close to the peak metamorphic condition.
399

400 **EVALUATION OF $\Delta\omega_1$ AND $\Delta\omega_2$**

401 The results presented in Figure 5 can explain the negative Raman frequency shifts of
402 quartz inclusion in Yanai Ryoke metamorphic rocks. Figure 10 shows the calculated
403 $\Delta\omega_1$ and $\Delta\omega_2$ values converted from the calculated residual pressure in Figure 5f using

Equations 4–7. The plausibility of Figure 10 is evaluated by comparing the measured frequency shifts of quartz Raman spectra in Yanai Ryoke metamorphic rocks and also by comparing the measured frequency shifts of quartz Raman spectra in high-pressure metamorphic rocks reported in previous studies.

In the samples of Yanai Ryoke metamorphic rocks, the maximum frequency shifts (lowest values of $\Delta\omega_1$ and $\Delta\omega_2$) of quartz inclusions of the samples from Chl-Bt, Ms-Crd, and Kfs-Crd zones are -4.5, -4.0, and -4.4 cm^{-1} for $\Delta\omega_1$ and -4.2, -3.1, and -4.1 cm^{-1} for $\Delta\omega_2$, respectively (Table 1). On the other hand, the calculated frequency shifts are at around -3.0 to -6.5 for $\Delta\omega_1$ and -3.5 to -7.5 for $\Delta\omega_2$ in the estimated metamorphic conditions of studied samples (Fig. 10). The measured $\Delta\omega_1$ and $\Delta\omega_2$ values are within the calculated $\Delta\omega_1$ and $\Delta\omega_2$ values except for the $\Delta\omega_2$ value of Ms-Crd zone, which is slightly higher than the calculated value. This difference might be attributable to the composition of garnet host (see the detailed discussion in **Chemical composition of garnet host**). The calculated $\Delta\omega_1$ and $\Delta\omega_2$ values in the case of spessartine host become 0.7 to 1.0 cm^{-1} higher than those in the case of almandine host, and the calculated $\Delta\omega_1$ and $\Delta\omega_2$ values using the thermodynamic dataset of spessartine are well consistent with the measured frequency shifts of Yanai Ryoke metamorphic rocks. Alternatively, the frequency of peak $E_{(128)}$ might not have been calibrated accurately because this peak is

422 distant from the calibration lines of a Ne lamp. In Figure 4, the line of $\Delta\omega_1$–$\Delta\omega_2$ does
423 not pass through the origin (0, 0), and $\Delta\omega_2$ values reaches 1.0 cm^{-1} at most. This means
424 that the wavenumber of the peak $E_{(128)}$, which affects the value of $\Delta\omega_2$, was lower than
425 that in the accurate condition. The results presented above imply that care is necessary
426 to constrain the metamorphic condition from $\Delta\omega_2$ value.
427 We also compared the positive frequency shifts reported in previous studies.
428 Kouketsu et al. (2010) reported $\Delta\omega_1$ of up to 11.8 cm^{-1} and $\Delta\omega_2$ of up to 13.8 cm^{-1} from
429 omphacite-bearing metapelite in the Sambagawa metamorphic belt, Southwest Japan.
430 The equilibrium metamorphic condition of this sample was estimated at 1.8–1.9
431 GPa/495–530 °C using the garnet–clinopyroxene–phengite assemblage (Krogh Ravna
432 and Terry 2004). In this metamorphic range, $\Delta\omega_1$ is calculated about 11–12 cm^{-1}, and
433 $\Delta\omega_2$ is about 13–14 cm^{-1} (Fig. 10), which shows good agreement with the measured
434 values. Endo et al. (2012) reported $\Delta\omega_1$ of up to 15.5 cm^{-1} and $\Delta\omega_2$ of up to 17.9 cm^{-1}
435 from lawsonite eclogite in the southern Motagua fault zone, Guatemala. The peak
436 metamorphic condition was estimated at 2.5 GPa/520 °C using pseudosection modeling
437 (Connolly 1990; Connolly 2009). The $\Delta\omega_1$ value is calculated 15.3 cm^{-1} and $\Delta\omega_2$ is 18.1
438 cm^{-1} in this estimated metamorphic condition (Fig. 10), which also shows good
439 agreement with the measured values.

The above discussions substantiate the accuracy of the calculation results in Figure 10. Although the negative range especially in $\Delta\omega_2$ requires further study, it has been clarified that the negative frequency shifts, i.e. negative residual pressure, of quartz inclusions in garnets occur when the quartz included in the host garnet under the metamorphic condition of low-*P/T* range without the phase transition of quartz.

IMPLICATIONS

We proposed a new technique to constrain the metamorphic condition applying the Raman spectroscopy to quartz inclusions in garnet hosts. The conventional geothermometry based on the thermodynamic calculations have problems that the mineral assemblage and their chemical compositions have been easily changed during the retrograde stage and the detection of peak metamorphic condition is difficult especially in highly recrystallized metamorphic rocks. In this study, we focused on the Raman spectroscopy that can detect the physical state of minerals, i.e. residual pressure in the inclusion–host system, which is less affected by the retrograde metamorphism than the conventional geothermometry. In particular, garnet tends to survive during the retrograde stage and the information obtained from its inclusion should reflect the earlier stage of garnet growth. This implies that the Raman spectroscopic analysis

458 combined with elastic modeling in this study can be used as a powerful and useful tool
459 to decipher information at prograde stage that was difficult for conventional method to
460 reveal even in highly recrystallized metamorphic rocks.

461

462 **ACKNOWLEDGEMENTS**

463 We are grateful to S. Wallis and H. Kagi for their constructive advice and to C.
464 Schmidt and anonymous referee for their careful reading and constructive suggestions,
465 which have led to considerable improvement of the manuscript. We also thank C.
466 Schmidt for providing unpublished data. The helpful editorial assistance of B.
467 Mihailova is also acknowledged. This study was financially supported by a Research
468 Fellowship for Young Scientists (Kouketsu: 22･7116) from the Japan Society for the
469 Promotion of Science (JSPS).

470

471 **REFERENCES CITED**

472 Ackermann, R.J. and Sorrell, C.A. (1974) Thermal expansion and the high-low
473 transformation in quartz. I. High-temperature X-ray studies. Journal of Applied
474 Crystallography, 7, 461–467.

475 Burnley, P.C. and Davis, M.K. (2004) Volume changes in fluid inclusions produced by
476 heating and pressurization: an assessment by finite element modeling. The Canadian
477 Mineralogist, 42, 1369–1382.
478 Burnley, P.C. and Schmidt, C. (2006) Finite element modeling of elastic volume
479 changes in fluid inclusions: Comparison with experiment. American Mineralogist,
480 91, 1807–1814.
481 Cao, Y., Song, S.G., Niu, Y.L., Jung, H., and Jin, Z.M. (2011) Variation of mineral
482 composition, fabric and oxygen fugacity from massive to foliated eclogites during
483 exhumation of subducted ocean crust in the North Qilian suture. Journal of
484 Metamorphic Geology, 29, 699–720.
485 Carpenter, M.A., Salje, E.K.H., Graeme-Barber, A., Wruck, B., Dove, M.T., and Knight,
486 K.S. (1998) Calibration of excess thermodynamic properties and elastic constant
487 variations associated with the alpha beta phase transition in quartz. American
488 Mineralogist, 83, 2–22.
489 Connolly, J.A.D. (1990) Multivariable phase diagrams: An algorithm based on
490 generalized thermodynamics. American Journal of Science, 290, 666–718.
491 Connolly, J.A.D. (2009) The geodynamic equation of state: What and how.
492 Geochemistry Geophysics Geosystems, 10, doi:10.1029/2009GC002540.

493 Dean, K.J., Sherman, W.F., and Wilkinson, G.R. (1982) Temperature and pressure
494 dependence of the Raman active modes of vibration of α-quartz. Spectrochimica
495 Acta Part A: Molecular Spectroscopy, 38, 1105–1108.
496 Dorogokupets, P.I. (1995) Equation of state for lambda transition in quartz. Journal of
497 Geophysical Research, 100, 8489–8499.
498 Enami, M., Nishiyama, T., and Mouri, T. (2007) Laser Raman microspectrometry of
499 metamorphic quartz: A simple method for comparison of metamorphic pressures.
500 American Mineralogist, 92, 1303–1315.
501 Endo, S., Wallis, S.R., Tsuboi, M., Torres De León, R., and Solari, L.A. (2012)
502 Metamorphic evolution of lawsonite eclogites from the southern Motagua fault zone,
503 Guatemala: insights from phase equilibria and Raman spectroscopy. Journal of
504 Metamorphic Geology, 30, 143–164.
505 Etchepare, J., Merian, M., and Smetankine, L. (1974) Vibrational normal modes of SiO_2.
506 I. α and β quartz. Journal of Chemical Physics, 60, 1873–1876.
507 Everall, N.J. (2000a) Modeling and measuring the effect of refraction on the depth
508 resolution of confocal Raman microscopy. Applied Spectroscopy, 54, 773–782.

509 Everall, N.J. (2000b) Confocal Raman microscopy: Why the depth resolution and
510 spatial accuracy can be much worse than you think. Applied Spectroscopy, 54,
511 1515–1520.
512 Fei, Y. (1995) Thermal Expansion, In T.J. Ahrens, Ed., Mineral Physics and
513 Crystallography: A Handbook of Physical Constants, 2, p. 29–44. American
514 Geophysical Union, Washington, D.C.
515 Gallivan, S.M. and Gupta, Y.M. (1995) Study of tensile deformation in shocked Z-cut,
516 α-quartz using time resolved Raman spectroscopy. Journal of Applied Physics, 78,
517 1557–1564.
518 Gillet, P., Ingrin, J., and Chopin, C. (1984) Coesite in subducted continental crust: *P–T*
519 history deduced from an elastic model. Earth and Planetary Science Letters, 70,
520 426–436.
521 Griggs, D. (1967) Hydrolytic weakening of quartz and other silicates. Geophysical
522 Journal of the Royal Astronomical Society, 14, 19–31.
523 Guiraud, M. and Powell, R. (2006) *P–V–T* relationships and mineral equilibria in
524 inclusions in minerals. Earth and Planetary Science Letters, 244, 683–694.
525 Hemley, R.J. (1987) Pressure dependence of Raman spectra of SiO_2 polymorphs;
526 α-quartz, coesite and stishovite. In H. Manghnani Murli and Y. Syono, Eds.,

527 High-pressure research in mineral physics, 39, p. 347–359. American Geophysical
528 Union, Washington, D.C.
529 Higashimoto, T., Nureki, I., Hara, E., Tsukuda, T., and Nakajima, T. (1983) Geology of
530 the Iwakuni district. Quadrangle Ser 1:50,000, Geol. Surv. Jpn, (in Japanese with
531 English abstract)
532 Holland, T.J.B. and Powell, R. (1998) An internally consistent thermodynamic data set
533 for phases of petrological interest. Journal of Metamorphic Geology, 16, 309–343.
534 Ikeda, T. (1993) Compositional zoning patterns of garnet during prograde
535 metamorphism from the Yanai District, Ryoke metamorphic belt, Southwest Japan.
536 Lithos, 30, 109–121.
537 Ikeda, T. (1998) Progressive sequence of reactions of the Ryoke metamorphism in the
538 Yanai district, southwest Japan: the formation of cordierite. Journal of Metamorphic
539 Geology, 16, 39–52.
540 Ikeda, T. (2004) Pressure-temperature conditions of the Ryoke metamorphic rocks in
541 Yanai district, SW Japan. Contributions to Mineralogy and Petrology, 146, 577–589.
542 Izraeli, E.S., Harris, J.W., and Navon, O. (1999) Raman barometry of diamond
543 formation. Earth and Planetary Science Letters, 173, 351–360.

Johnson, E.A. (2006) Water in nominally anhydrous crustal minerals: speciation, concentration, and geologic significance. Reviews in mineralogy and geochemistry, 62, 117–154.

Jorgensen, J.D. (1978) Compression mechanisms in α-quartz structures—SiO_2 and GeO_2. Journal of Applied Physics, 49, 5473–5478.

Kagi, H., Odake, S., Fukura, S., and Zedgenizov, D.A. (2009) Raman spectroscopic estimation of depth of diamond origin: technical developments and the application. Russian Geology and Geophysics, 50, 1183–1187.

Katayama, I., Zayachkovsky, A.A., and Maruyama, S. (2000) Prograde pressure-temperature records from inclusions in zircons from ultrahigh-pressure-high-pressure rocks of the Kokchetav Massif , northern Kazakhstan. Island Arc, 9, 417–427.

Kouketsu, Y., Enami, M., and Mizukami, T. (2010) Omphacite-bearing metapelite from the Besshi region, Sambagawa metamorphic belt, Japan: Prograde eclogite facies metamorphism recorded in metasediment. Journal of Mineralogical and Petrological Sciences, 105, 9–19.

Krogh Ravna, E.J., and Terry, M.P. (2004) Geothermobarometry of UHP and HP eclogites and schists–an evaluation of equilibria among

garnet–clinopyroxene–kyanite–phengite–coesite/quartz. Journal of Metamorphic Geology, 22, 579–592.

Miyashiro, A. (1961) Evolution of metamorphic belts. Journal of Petrology, 2, 277–311.

Nasdala, L., Hofmeister, W., Harris, J.W., and Glinnemann, J. (2005) Growth zoning and strain patterns inside diamond crystals as revealed by Raman maps. American Mineralogist, 90, 745–748.

Nishiyama, T. and Aikawa K. (2011) Implication of the residual pressure recorded in quartz inclusions in garnet from high *T* metamorphic terranes. Japan Geoscience Union Meeting Abstract 2011, SMP046-05.

Ogata, K., Takeuchi, Y., and Kudoh, Y. (1987) Structure of α-quartz as a function of temperature and pressure. Zeitschrift für Kristallographie, 179, 403–413.

Parkinson, C.D. and Katayama, I. (1999) Present-day ultrahigh-pressure conditions of coesite inclusions in zircon and garnet: Evidence from laser Raman microspectroscopy. Geology, 27, 979–982.

Pavese, A., Diella, V., Pischedda, V., Merli, M., Bocchio, R., and Mezouar, M. (2001) Pressure–volume–temperature equation of state of andradite and grossular, by high-pressure and-temperature powder diffraction. Physics and Chemistry of Minerals, 28, 242–248.

580 Plymate, T.G. and Stout, J.H. (1989) A five-parameter temperature-corrected Murnaghan
581 equation for P-V-T surfaces. Journal of Geophysical Research, 94, 9477–9483.
582 Rossman, G.R. (1990) Hydrogen in “anhydrous” minerals. Nuclear Instruments and
583 Methods in Physics Research B, 45, 41–44.
584 Sato, K., Santosh, M., and Tsunogae, T. (2009) A petrologic and laser Raman
585 spectroscopic study of sapphirine–spinel–quartz–Mg-staurolite inclusions in garnet
586 from Kumiloothu, southern India: Implications for extreme metamorphism in a
587 collisional orogen. Journal of Geodynamics, 47, 107–118.
588 Schmidt, C. and Ziemann, M.A. (2000) In-situ Raman spectroscopy of quartz: A
589 pressure sensor for hydrothermal diamond-anvil cell experiments at elevated
590 temperatures. American Mineralogist, 85, 1725–1734.
591 Shen, A.H., Bassett, W.A., and Chou, I.-M. (1993) The α-β quartz transition at high
592 temperatures and pressures in a diamond-anvil cell by laser interferometry.
593 American Mineralogist, 78, 694–698.
594 Sobolev, N.V., Fursenko, B. A, Goryainov, S.V., Shu, J., Hemley, R.J., Mao, H.-K., and
595 Boyd, F.R. (2000) Fossilized high pressure from the Earth’s deep interior: the
596 coesite-in-diamond barometer. Proceedings of the National Academy of Sciences of
597 the United States of America, 97, 11875–11879.

598 Suzuki, K. and Adachi, M. (1998) Denudation history of the high *T/P* Ryoke
599 metamorphic belt, southwest Japan: constraints from CHIME monazite ages of
600 gneisses and granitoids. Journal of Metamorphic Geology, 16, 23–37.
601 Tsunogae, T. and Santosh, M. (2006) Spinel–sapphirine–quartz bearing composite
602 inclusion within garnet from an ultrahigh-temperature pelitic granulite: Implications
603 for metamorphic history and *P–T* path. Lithos, 92, 524–536.
604 Van der Molen, I. (1981) The shift of the α-β transition temperature of quartz associated
605 with the thermal expansion of granite at high pressure. Tectonophysics, 73,
606 323–342.
607 Van der Molen, I. and Van Roermund, H.L.M. (1986) The pressure path of solid
608 inclusions in minerals: the retention of coesite inclusions during uplift. Lithos, 19,
609 317–324.
610 Wang, Z. and Ji, S. (2001) Elasticity of six polycrystalline silicate garnets at pressure up
611 to 3.0 GPa. American Mineralogist, 86, 1209–1218.
612 Whitney, D.L., Lang, H.M., and Ghent, E.D. (1995) Quantitative determination of
613 metamorphic reaction history: mass balance relations between groundmass and
614 mineral inclusion assemblages in metamorphic rocks. Contributions to Mineralogy
615 and Petrology, 120, 404–411.

Zhang, L., Ahsbahs, H., Kutoglu, A., and Geiger, C.A. (1999) Single-crystal hydrostatic compression of synthetic pyrope, almandine, spessartine, grossular and andradite garnets at high pressures. Physics and Chemistry of Minerals, 27, 52–58.

Zhang, Y. (1998) Mechanical and phase equilibria in inclusion–host systems. Earth and Planetary Science Letters, 157, 209–222.

FIGURE CAPTIONS

FIGURE 1. Map of metamorphic zones of the Ryoke metamorphic rocks in the Yanai district, Southwest Japan, with sample localities. Abbreviations: Chl zone, chlorite zone; Chl-Bt zone, chlorite-biotite zone; Ms-Crd zone, muscovite-cordierite zone; Kfs-Crd zone, K-feldspar-cordierite zone; Grt-Crd zone, garnet-cordierite zone; Sil-Kfs zone, sillimanite-K-feldspar zone; MTL, Median Tectonic Line.

FIGURE 2. Representative Raman spectra of α-quartz at atmospheric pressure and room temperature. Symbols on the peaks are vibration mode in α-quartz. Numbers in parentheses are the frequency of standard quartz. The direction of frequency shift of each peak corresponding to the compression (C) and tension (T) is indicated by small arrows. The extents of frequency shifts are expressed as ω_1 and ω_2.

633 **FIGURE 3.** Photomicrographs of quartz inclusions in garnet hosts. (a) Chl-Bt zone, (b)
634 Ms-Crd zone, and (c) Kfs-Crd zone.

635 **FIGURE 4.** $\Delta\omega_1$ vs. $\Delta\omega_2$, which are the parameters of frequency shifts of quartz Raman
636 spectra. (a) Chl-Bt zone, (b) Ms-Crd zone, and (c) Kfs-Crd zone.

637 **FIGURE 5.** Calculated volume changes of quartz (a–c) and residual pressures (d–f) in
638 the range of 0.1MPa–2.6 GPa/25–600 °C. References of equation of states (EOS) and
639 thermoelastic parameters of quartz (Parameter) used in the calculations are shown in the
640 upper part. The gray areas in (d), (e), and (f) represent the negative residual pressure
641 ranges.

642 **FIGURE 6.** Relation between pressure (*P*; GPa) and frequency shifts ($\Delta\omega_1$ and
643 $\Delta\omega_2$; cm^{-1}) at 23 °C in the experiment of Schmidt and Ziemann (2000). The negative
644 range was extrapolated from the lower compressional range.

645 **FIGURE 7.** (a), (b) Frequency shifts ($\Delta\omega_1$ and $\Delta\omega_2$) vs. quartz grain size. (c), (d)
646 Frequency shifts vs. quartz grain shape. The mean grain size was calculated as $\sqrt{ab}$
647 and grain shape as *b/a*, where *a* and *b* are longest and shortest lengths of quartz
648 inclusion.

649 **FIGURE 8.** Calculated residual pressure (P_i) vs. metamorphic pressure (P_0) considering
650 the effect of radii of inclusion quartz (R_i) and host garnet (R_h) at T_0 = 500 and 600 °C. x
651 = R_i^3 / R_h^3.

652 **FIGURE 9.** Calculated residual pressure (P_i) vs. metamorphic pressure (P_0) in the case
653 of four garnet end-members (almandine, pyrope, grossular, and spessartine) at T_0 = 500
654 and 600 °C.

655 **FIGURE 10.** Calculated $\Delta\omega_1$ and $\Delta\omega_2$ values of quartz inclusion in garnet in the range
656 of 0.1MPa–2.6 GPa/25–600 °C. The $\Delta\omega_1$ and $\Delta\omega_2$ values are converted from P_i in
657 Figure 5f. The estimated metamorphic conditions in previous studies, Kouketsu et al.
658 (2010) and Endo et al. (2012), are shown as open square and star, respectively. The
659 metamorphic P–T conditions of Yanai Ryoke metamorphic rocks used in the present
660 study are shown as gray squares. The gray areas represent the negative residual pressure
661 ranges.

TABLE 1. Estimated metamorphic conditions and maximum frequency shifts of Raman spectrum of quartz in garnet of the Yanai Ryoke metamorphic rocks used in the present study.

Sample no.	Zone	*P* (GPa)	*T* (°C)	$\Delta\nu_{A1(464)}$ (cm^{-1})	$\Delta\nu_{A1(205)}$ (cm^{-1})	$\Delta\nu_{E(127)}$ (cm^{-1})	$\Delta\omega_1$ (cm^{-1})	$\Delta\omega_2$ (cm^{-1})
YEB5	Chl-Bt	0.08 ±0.1	492 ±35	-1.6	-6.1	-1.9	-4.5	-4.2
YBB7	Ms-Crd	0.19 ±0.1*	551 ±35*	-2.2	-6.2	-3.1	-4.0	-3.1
YMA5	Ms-Crd	0.19 ±0.1*	551 ±35*	-0.3	-3.5	-0.7	-3.2	-2.8
YMA10	Ms-Crd	0.19 ±0.1*	551 ±35*	-0.6	-3.4	-1.7	-2.9	-1.7
YAF16	Kfs-Crd	0.26 ±0.1	594 ±35	-2.1	-6.0	-3.0	-3.9	-3.0
YAF19	Kfs-Crd	0.27 ±0.1	590 ±35	-2.0	-6.4	-2.3	-4.4	-4.1

*Estimated condition of the sample YBB6 that was collected within 200m apart from samples YBB7, YMA5, and YMA10.

TABLE 2. Comparison of thermal expansion coefficient (α), thermal expansion parameter ($a°$), bulk modulus (κ), and shear modulus (μ) of garnet end members and quartz at standard condition (0.1 MPa and 298 K).

Mineral	$\alpha \times 10^{-5}$ (K^{-1})	$a° \times 10^{-5}$ (K^{-1})	κ (GPa)	μ (GPa)
Garnet				
Almandine	1.70	4.03[1]	169.0[1]	
	1.57[2]	3.73	175.1[3]	92.1[3]
Pyrope	1.83	4.36[1]	173.7[1]	
	1.98[2]	4.71	170.1[3]	90.2[3]
Grossular	1.65	3.93[1]	168.0[1]	
	1.63[2]	3.87	166.3[3]	98.1[3]
Sperssartine	1.94	4.62[1]	179.0[1]	
	1.71[2]	4.06	171.8[3]	93.3[3]
Quartz	0.27	0.65[1]	75.0[1]	
	2.38[2]	5.66		
	3.13[4]	7.44	37.3[4]	
	3.53[5]	8.38	37.1[5]	

[1] Holland and Powell (1998); [2] Fei (1995); [3] Wang and Ji (2001);
[4] Plymate and Stout (1989); [5] Dorogokupets (1995)

APPENDIX TABLE 1. Representative analyses of the garnets. Samples YEB5, YBB7, and YAF19 were collected from the Ryoke belt in the Yani district, ZWK02 was collected from the Sambagawa belt, and GM13 was collected from the Motagua fault zone.

Sample	YEB5[1]	YBB7[2]	YAF19[1]	ZWK02[3]	GM13[4]
	Chl-Bt	Ms-Crd	Kfs-Crd	Sambagawa belt	Motagua Fault zone
SiO_2 (wt.%)	36.89	37.12	36.89	37.60	37.18
Al_2O_3	20.92	20.94	20.69	20.70	20.30
FeO	14.49	24.51	25.27	26.00	31.97
MnO	25.00	13.44	15.05	2.52	0.49
MgO	1.17	1.47	2.46	1.34	2.37
CaO	0.78	1.85	0.76	11.80	7.00
Total	99.25	99.33	101.12	99.96	99.31
Si (pfu)	3.02	3.02	2.98	3.00	3.00
Al	2.02	2.01	1.97	1.95	1.93
Fe	0.99	1.67	1.71	1.73	2.16
Mn	1.73	0.93	1.03	0.17	0.03
Mg	0.14	0.18	0.30	0.16	0.29
Ca	0.07	0.16	0.07	1.01	0.61
Total	7.97	7.97	8.04	8.01	8.02
X_{Alm}	0.34	0.57	0.55	0.56	0.70
X_{Prp}	0.05	0.06	0.10	0.05	0.09
X_{Grs}	0.02	0.05	0.02	0.33	0.20
X_{Sps}	0.59	0.32	0.33	0.06	0.01

[1] Ikeda (2004); [2] Ikeda (1993); [3] Kouketsu et al. (2010); [4] Endo et al. (2012)

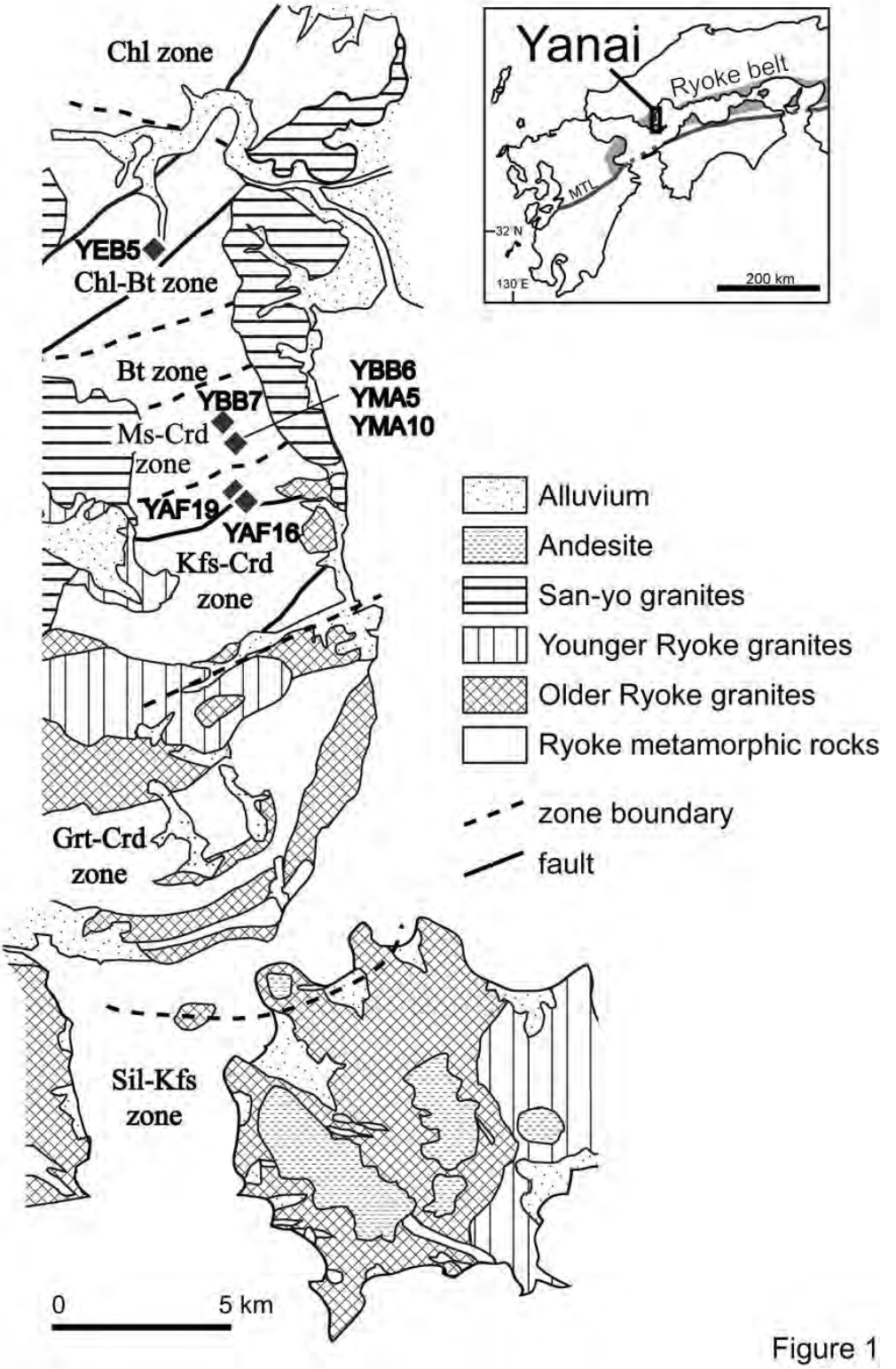
Chl zone
YEB5
Chl-Bt zone
Bt zone
YBB7
YBB6
YMA5
YMA10
Ms-Crd zone
YAF19
YAF16
Kfs-Crd zone
Grt-Crd zone
Sil-Kfs zone
0
5 km
Yanai
Ryoke belt
MTL
32°N
130°E
200 km
Alluvium
Andesite
San-yo granites
Younger Ryoke granites
Older Ryoke granites
Ryoke metamorphic rocks
zone boundary
fault

Figure 1

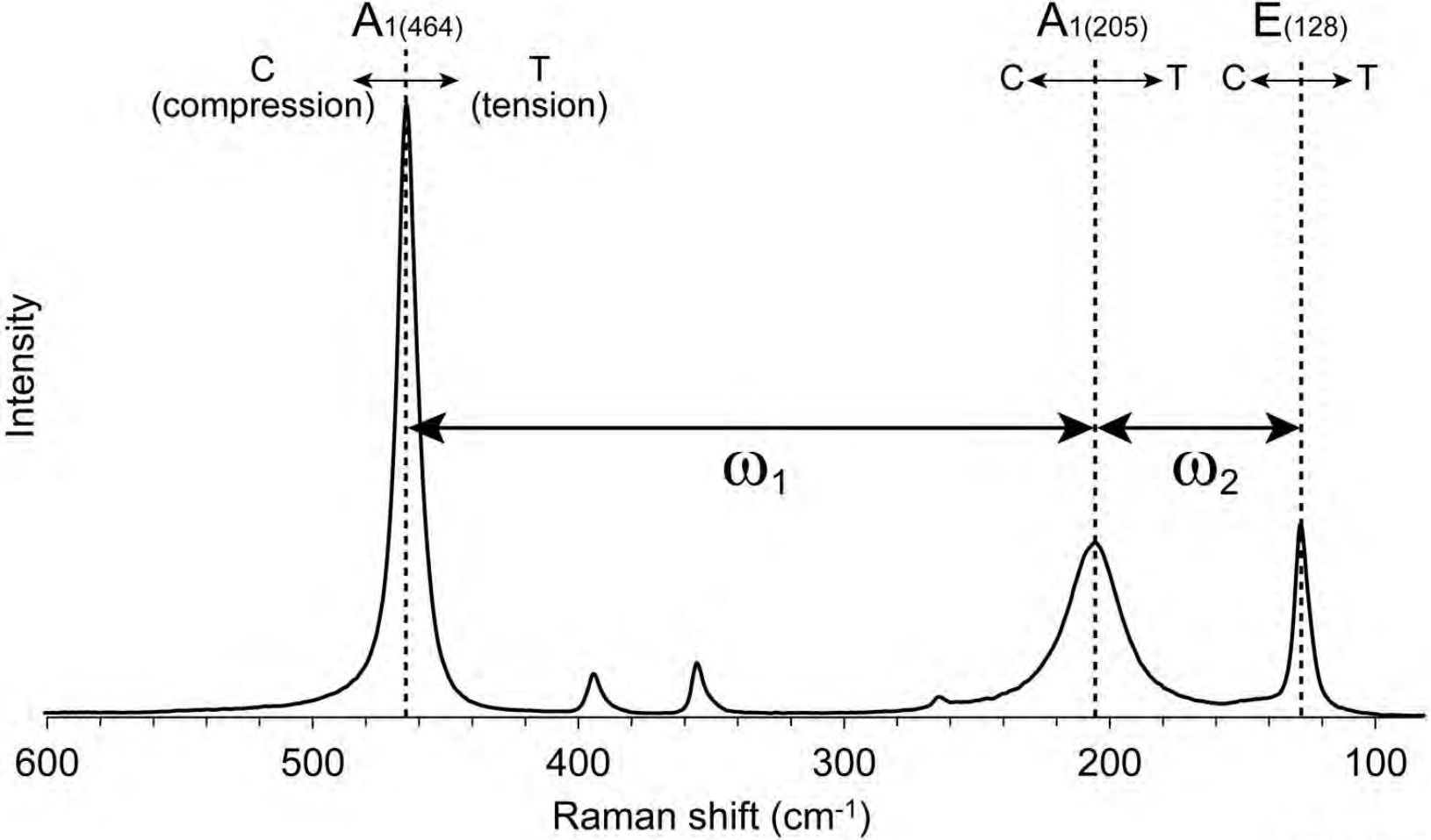
A1(464)
C
(compression)
T
(tension)
A1(205)
C
T
E(128)
C
T
Intensity
ω1
ω2
600
500
400
300
200
100
Raman shift (cm-1)

Figure 2

(a) Chl-Bt

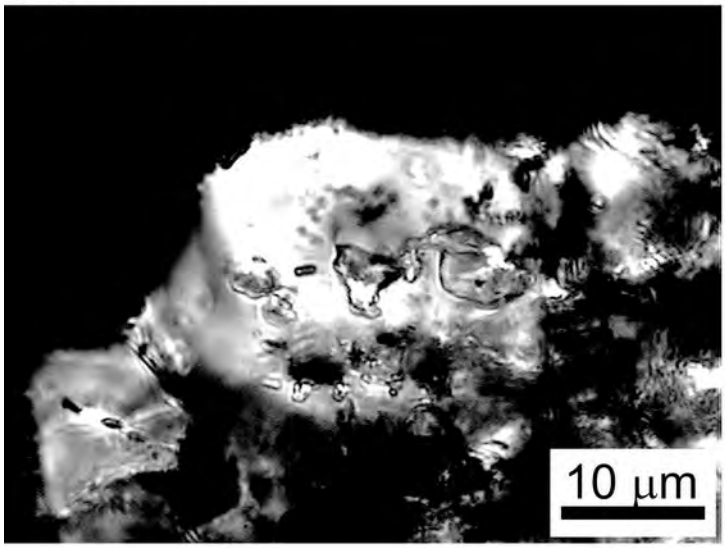

(b) Ms-Crd

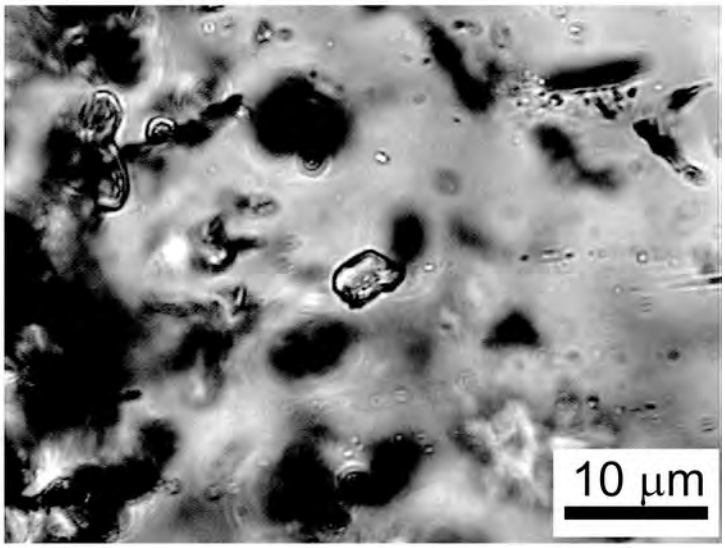

(c) Kfs-Crd

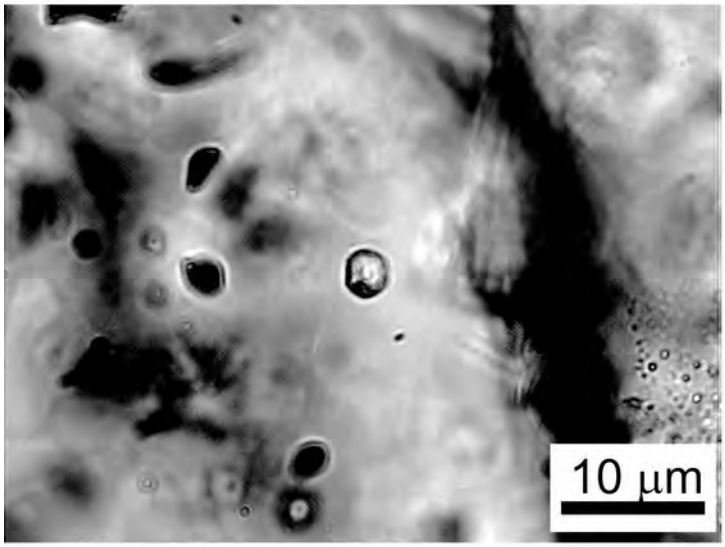

Figure 3

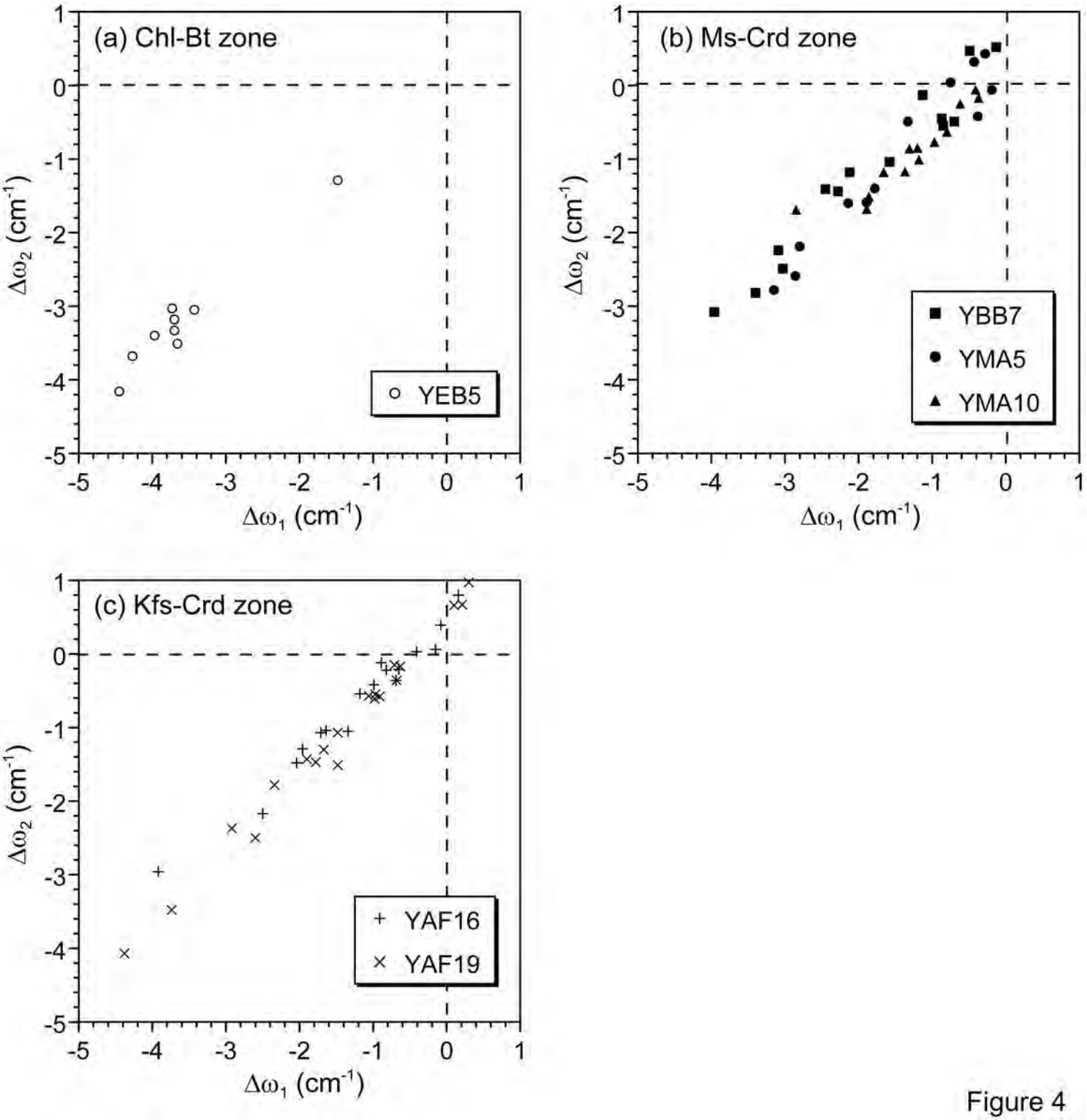
(a) Chl-Bt zone
YEB5
(b) Ms-Crd zone
YBB7
YMA5
YMA10
(c) Kfs-Crd zone
YAF16
YAF19
Δω2 (cm-1)
Δω1 (cm-1)

Figure 4

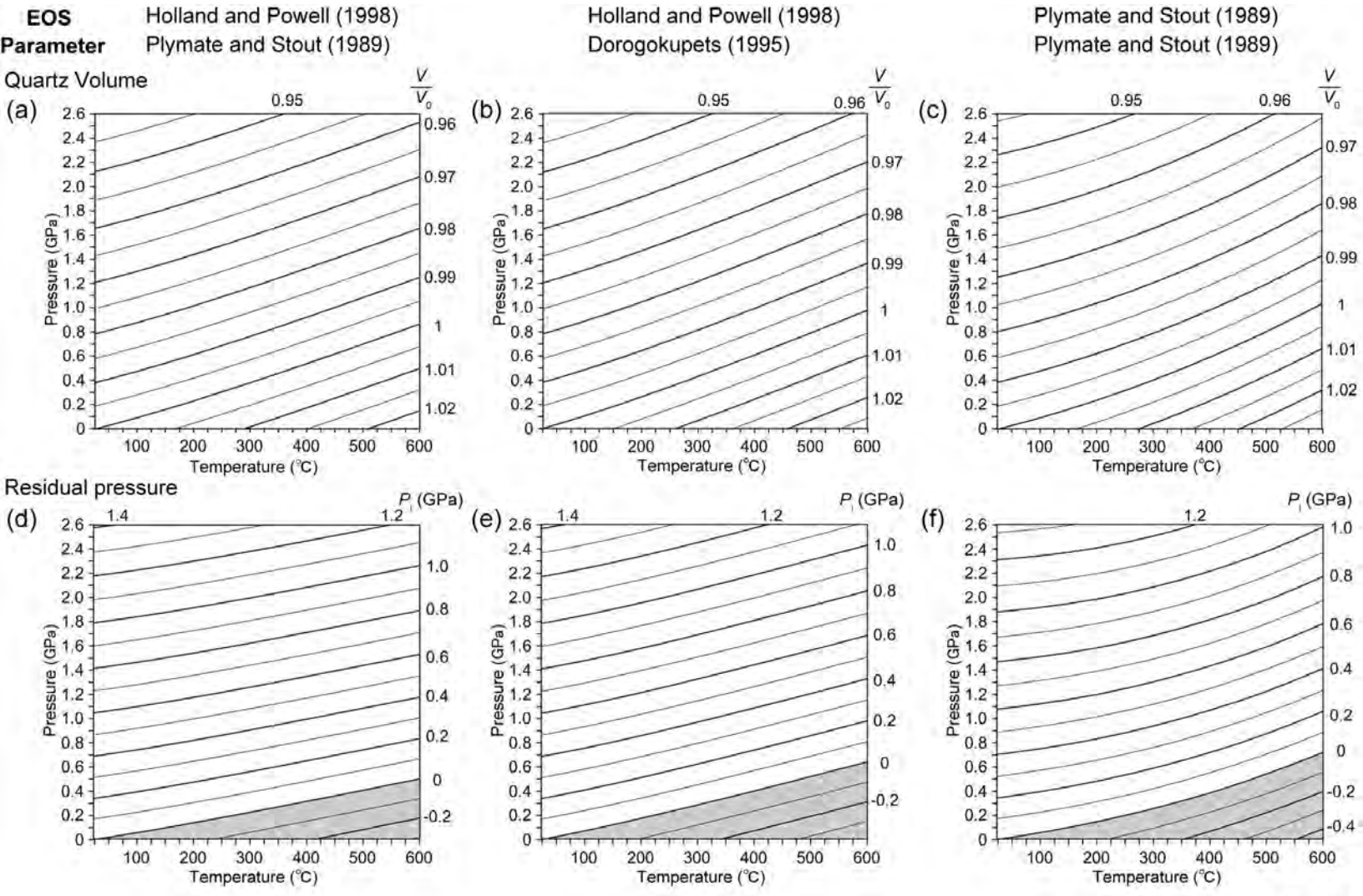
EOS
Parameter
Holland and Powell (1998)
Plymate and Stout (1989)
Holland and Powell (1998)
Dorogokupets (1995)
Plymate and Stout (1989)
Plymate and Stout (1989)
Quartz Volume
(a)
(b)
(c)
V/V0
Pressure (GPa)
Temperature (°C)
Residual pressure
(d)
(e)
(f)
Pr (GPa)

Figure 5

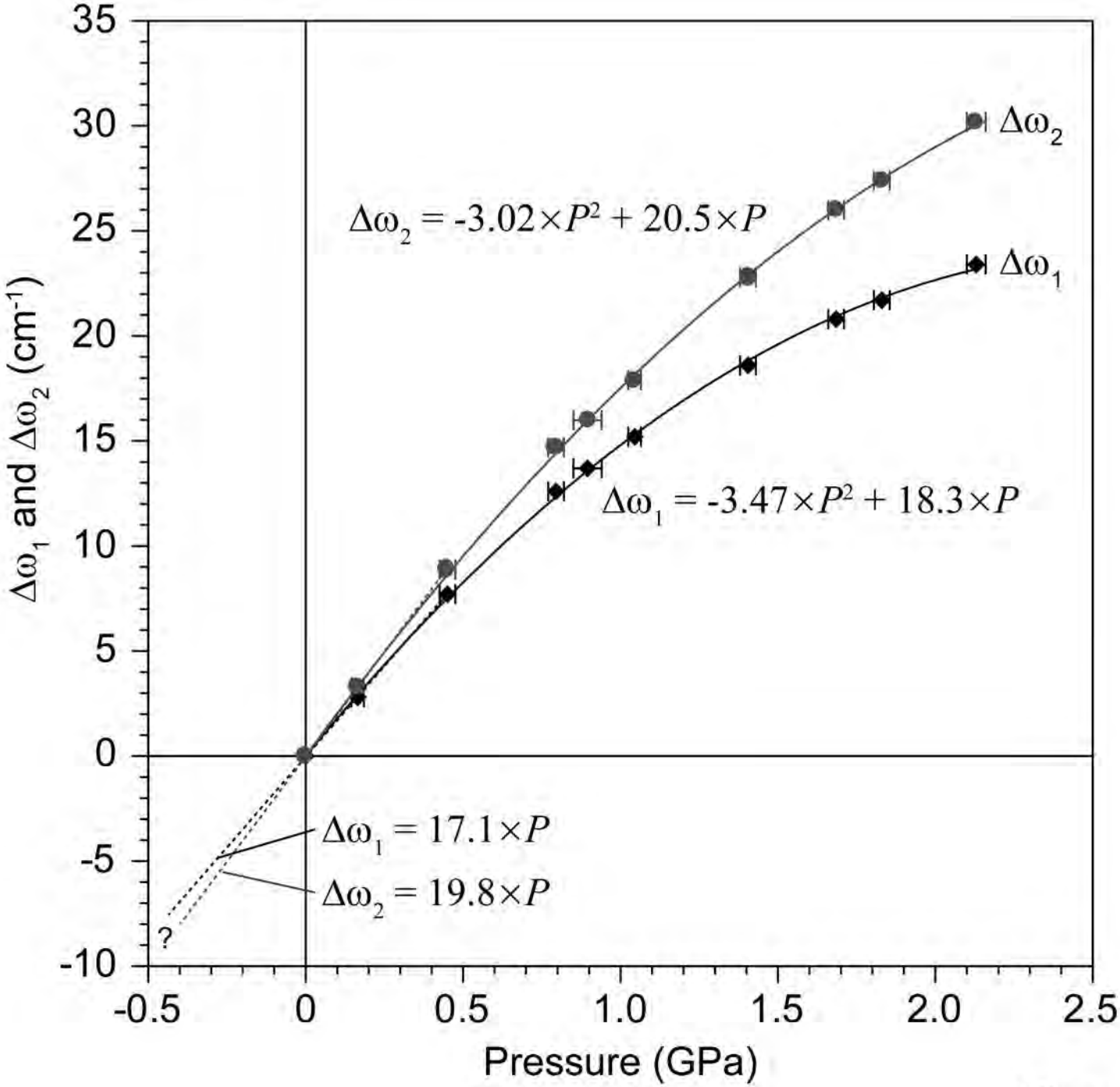
35
30
25
20
15
10
5
0
-5
-10
-0.5
0
0.5
1.0
1.5
2.0
2.5
Pressure (GPa)
Δω1 and Δω2 (cm-1)
Δω2
Δω1
Δω2 = -3.02×P2 + 20.5×P
Δω1 = -3.47×P2 + 18.3×P
Δω1 = 17.1×P
Δω2 = 19.8×P
?

Figure 6

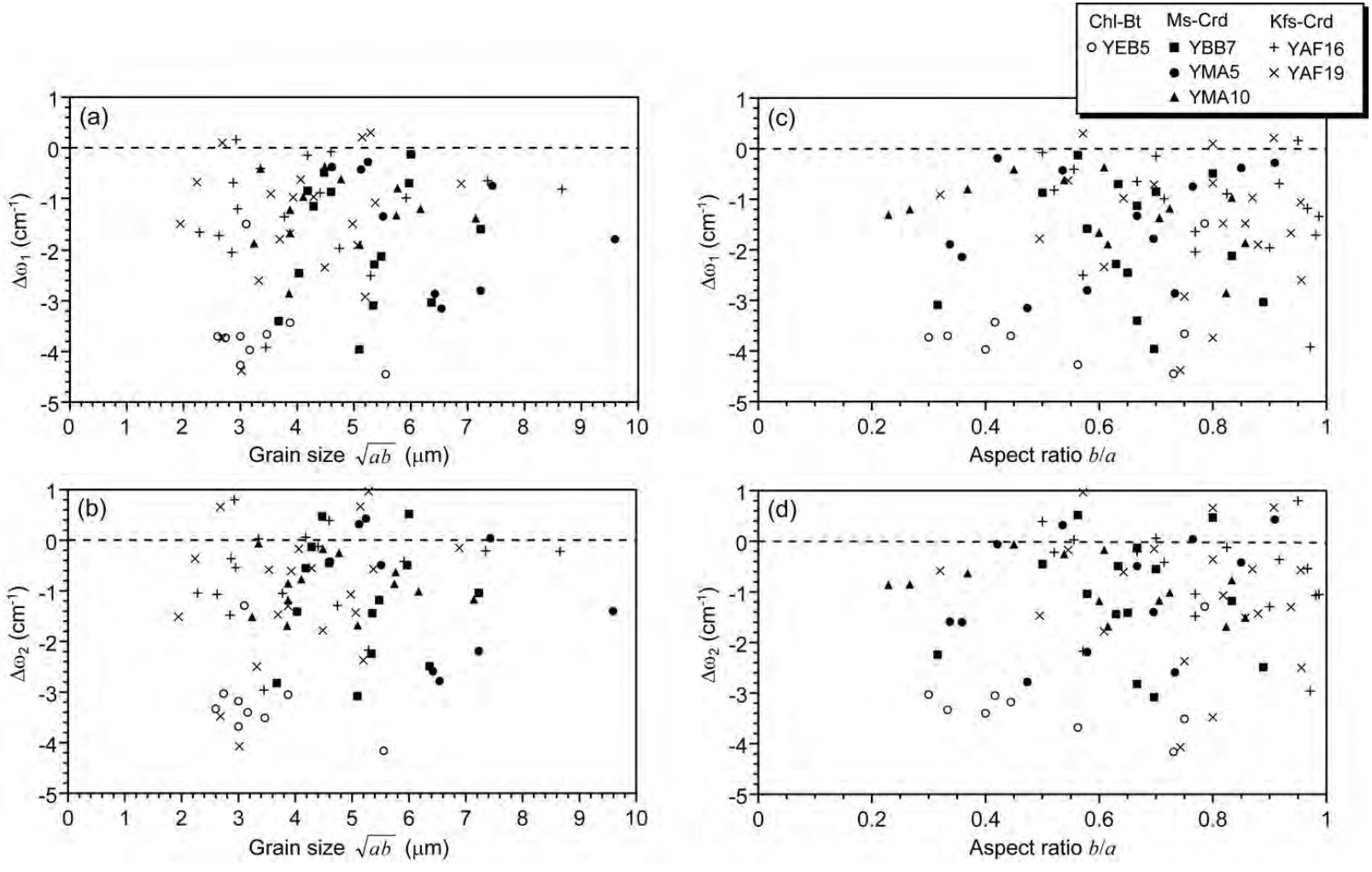
Chl-Bt
YEB5
Ms-Crd
YBB7
YMA5
YMA10
Kfs-Crd
YAF16
YAF19
(a)
(b)
(c)
(d)
Δω1 (cm-1)
Δω2 (cm-1)
Grain size √ab (μm)
Aspect ratio b/a

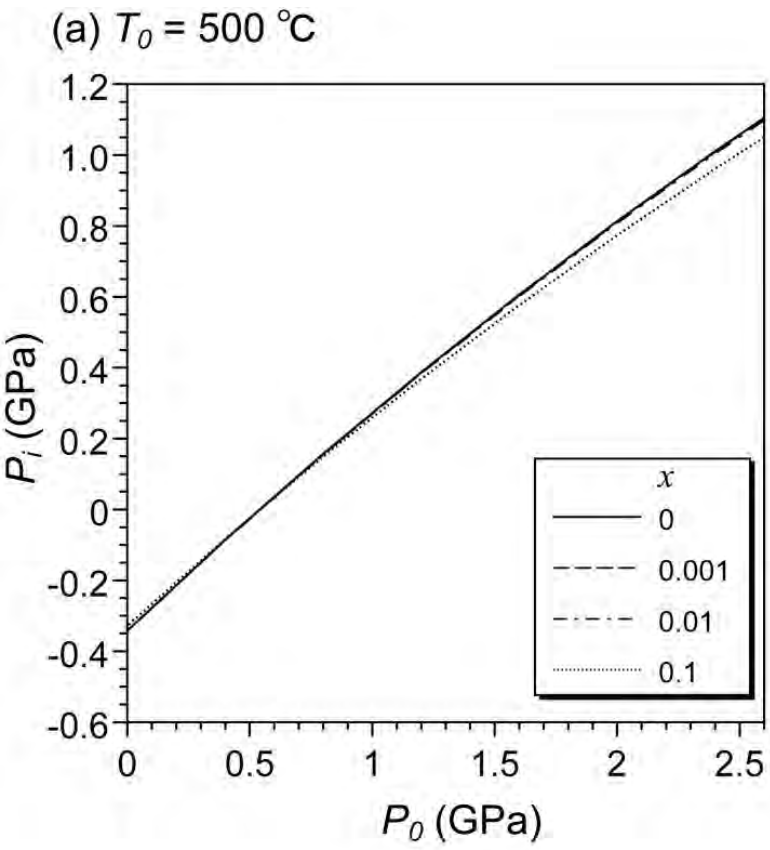
(a) T_0 = 500 ℃
1.2
1.0
0.8
0.6
0.4
0.2
0
-0.2
-0.4
-0.6
P_i (GPa)
0
0.5
1
1.5
2
2.5
P_0 (GPa)
x
0
0.001
0.01
0.1

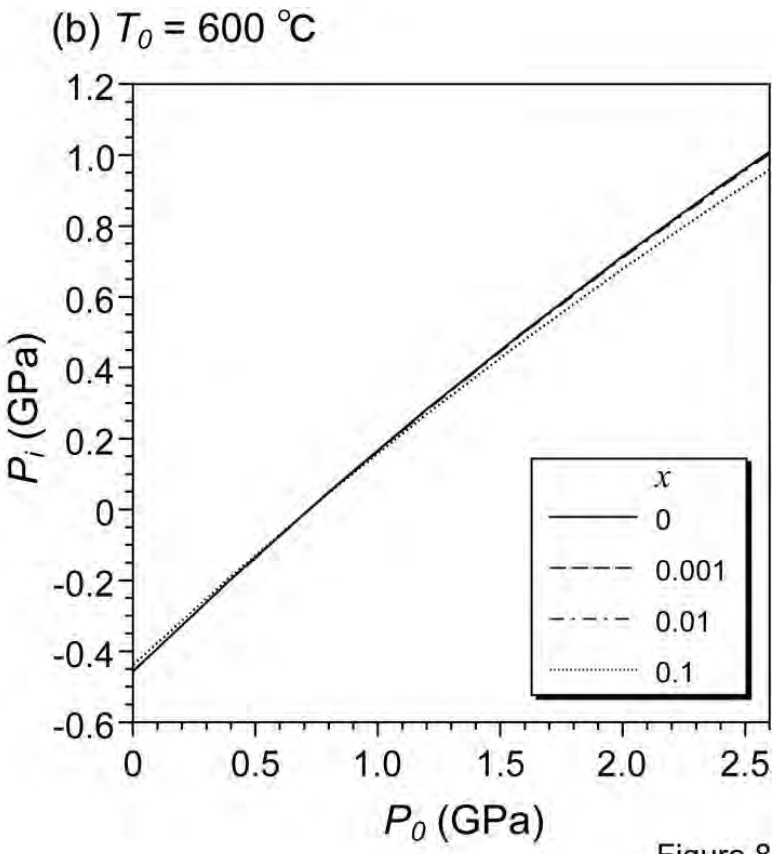
(b) T_0 = 600 ℃
1.2
1.0
0.8
0.6
0.4
0.2
0
-0.2
-0.4
-0.6
P_i (GPa)
0
0.5
1.0
1.5
2.0
2.5
P_0 (GPa)
x
0
0.001
0.01
0.1

Figure 8

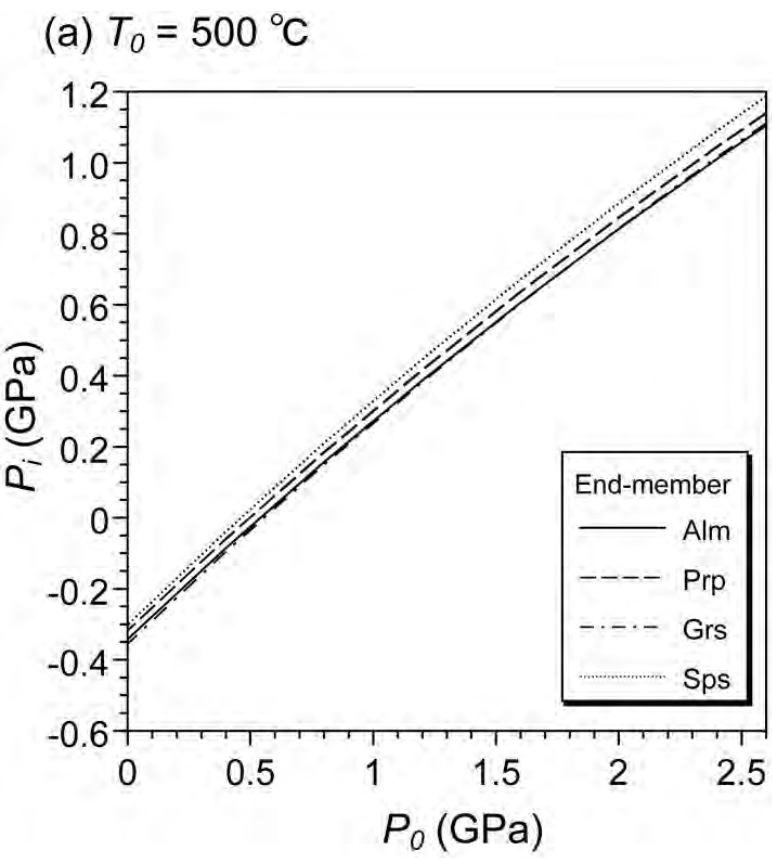
(a) T_0 = 500 ℃
1.2
1.0
0.8
0.6
0.4
0.2
0
-0.2
-0.4
-0.6
P_i (GPa)
0
0.5
1
1.5
2
2.5
P_0 (GPa)
End-member
Alm
Prp
Grs
Sps

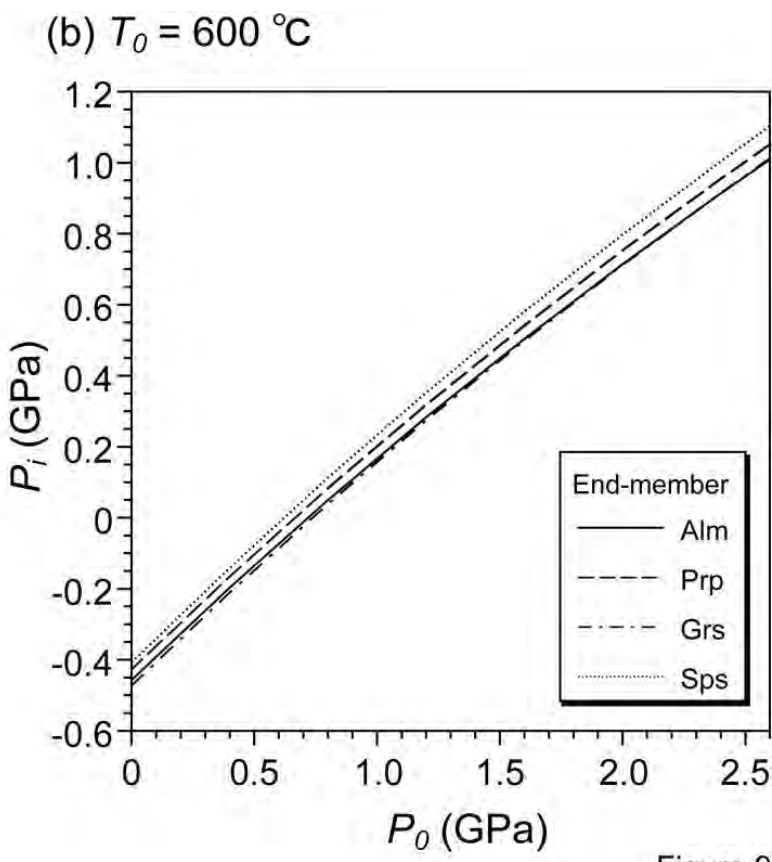
(b) T_0 = 600 ℃
1.2
1.0
0.8
0.6
0.4
0.2
0
-0.2
-0.4
-0.6
P_i (GPa)
0
0.5
1.0
1.5
2.0
2.5
P_0 (GPa)
End-member
Alm
Prp
Grs
Sps

Figure 9

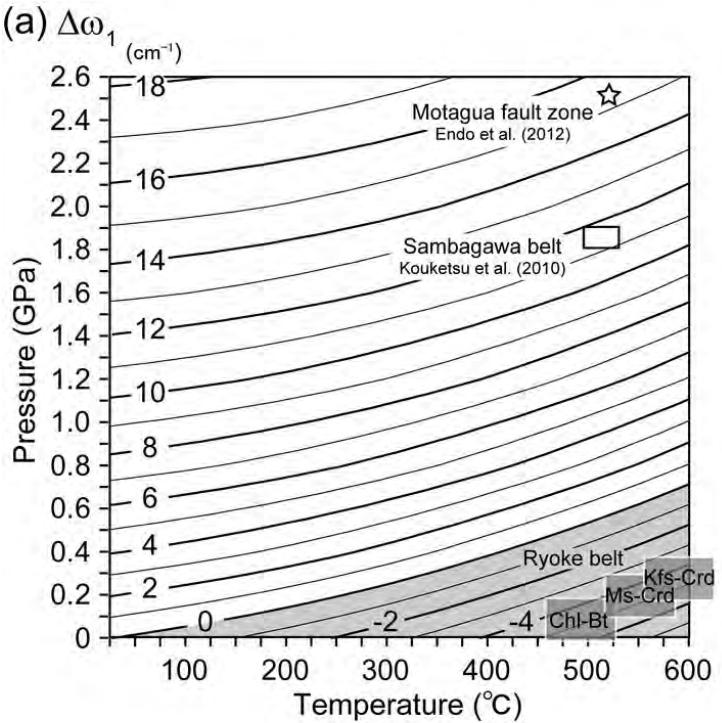
(a) Δω1 (cm⁻¹)
Pressure (GPa)
Temperature (°C)
Motagua fault zone
Endo et al. (2012)
Sambagawa belt
Kouketsu et al. (2010)
Ryoke belt
Kfs-Crd
Ms-Crd
Chl-Bt
18
16
14
12
10
8
6
4
2
0
-2
-4

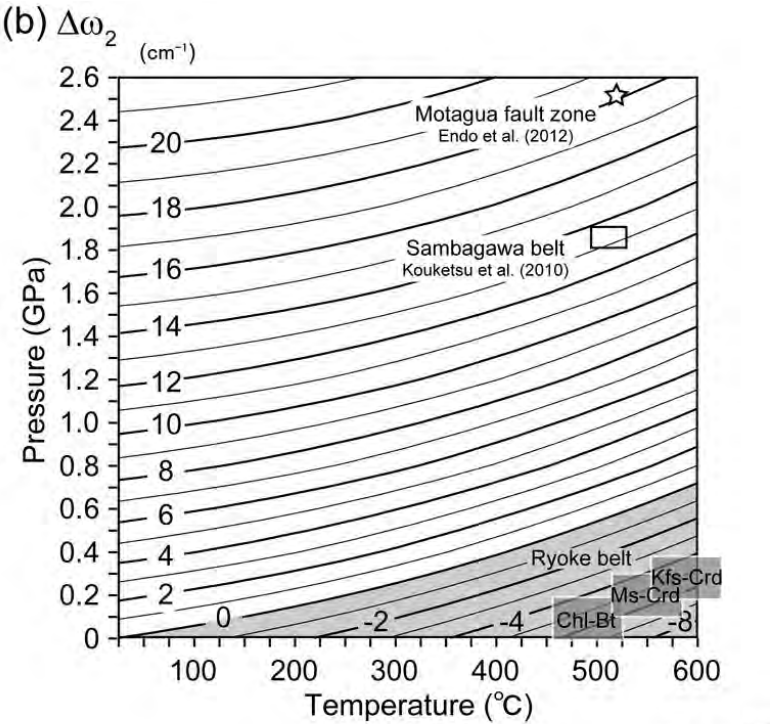
(b) Δω2 (cm⁻¹)
Pressure (GPa)
Temperature (°C)
Motagua fault zone
Endo et al. (2012)
Sambagawa belt
Kouketsu et al. (2010)
Ryoke belt
Kfs-Crd
Ms-Crd
Chl-Bt
20
18
16
14
12
10
8
6
4
2
0
-2
-4
-8

Figure 10